Highly Reversible Na-Intercalation into Graphite Recovered from Spent Li–Ion Batteries for High-Energy Na-Ion Capacitor

Madhusoodhanan Lathika Divya[+],[a] Subramanian Natarajan[+],[a] Yun-Sung Lee,[b] and Vanchiappan Aravindan*[a]

High-performance Na-ion capacitor (NIC) was constructed with graphite recovered from spent Li-ion batteries (LIBs) as battery-type negative electrode and high-surface-area activated carbon as a supercapacitor component. Unlike Li-insertion into graphite, Na-insertion into graphite is extremely limited; hence, a "solvent-co-intercalation" mechanism was proposed for high reversibility using ether family solvents. First, the Na-insertion properties were assessed in the half-cell assembly with 0.5 M $NaPF_6$ in tetraethylene glycol dimethyl ether as an electrolyte solution and compared with the commercial graphite. The NIC comprised pre-sodiated graphite as a negative electrode and commercial activated carbon as a cathode. This fascinating NIC configuration displayed the maximum energy density of 59.93 Wh kg^{-1} with exceptional cyclability of 5000 cycles at ambient temperature with approximately 98% retention. Interestingly, the electrode aging process in the presence of electrolyte resulted in approximately 19% higher energy density than the routine electrode heat treatment. Further, the electrochemical activity of the NIC at various temperatures was studied, and it was found that the graphite recovered from spent LIBs could be effectively reused towards the construction of high-performance charge storage devices with exceptional performance.

Introduction

The demand for clean, low-cost, and efficient energy storage systems (ESS) is increasing tremendously to meet the requirements for various electric systems and, in addition, to reach the desired targets in the electric vehicle (EV) sector in a feasible way.[1] Hybrid capacitors are the effective combination of lithium-ion batteries (LIBs) and supercapacitors (electric double-layer capacitors, EDLCs), which provide a higher energy density than EDLCs as well as higher durability than LIBs.[2] Furthermore, hybrid capacitors can be considered as a safer substitute to LIBs by acquiring higher energy and power density within a single system. However, the main downside to lithium is increasing shortage in the near future that could develop because of the augmented demand of EVs (≈4 kg Li per battery), and also because of its limited resource.[3] Similarly, the usage of LIBs in ESS is circumscribed by overpriced Li, which paved the way to discover sodium (Na), which belongs to the first group, as an alternative to Li with similar intercalation chemistry. Recently, research in Na-ion batteries (NIBs) and Na-ion capacitors (NICs) has received increased attention due to its abundant resource and the low-cost system as compared to Li. The amount of sodium in the Earth's crust and water reaches to 28400 mg kg^{-1} and 11000 mg L^{-1} compared to 20 mg kg^{-1} and 0.18 mg L^{-1} for Li.[4] Moreover, Al encounters alloying reaction with Li at approximately 0.5 V vs. Li/Li^+, whereas Na does not react with aluminum. Therefore, the expensive Cu current collector can be swapped with Al in Na-based energy storage systems. Besides, NICs having similar configurations as Li-ion capacitors (LIC) with activated carbon (AC) cathode and battery type anode paves a way to explore advanced NIC in a cost-effective technique.

However, Li cannot be simply replaced with Na as there are some noticeable differences between these two systems. Especially, Na^+ ions have larger ion size (1.02 Å vs. 0.76 Å for Li^+ ions), higher standard electrode potential vs. standard hydrogen electrode (−2.71 V vs. −3.02 V for Li), and also higher density than Li (23 g mol^{-1} vs. 6.9 g mol^{-1} for Li).[5] The charge storage mechanism of NIC is based on the reversible anion adsorption/desorption on the surface of the capacitive-type electrode and reversible intercalation/de-intercalation of Na^+ ions in the battery-type electrode. However, the energy density of NICs is not reaching the desired level, which can be due to sluggish redox reaction kinetics because of the large size of Na^+ ions and also a result of changes in the structure of electrode material during the charge-discharge process. Besides, most of the electrode materials (anode) for LICs are not suitable for NICs because of the large size of Na^+ ions and higher ionization potential. For that reason, NICs require wide attention to find a suitable host material for Na^+ ions in combination with different electrolytes.

[a] M. L. Divya,[+] Dr. S. Natarajan,[+] Dr. V. Aravindan
Department of Chemistry
Indian Institute of Science Education and Research (IISER)
Tirupati 517507 (India)
E-mail: aravind_van@yahoo.com
[b] Prof. Y.-S. Lee
Department of Advanced Chemicals and Engineering
Chonnam National University
Gwang-ju 61186 (Republic of Korea)
[+] These authors contributed equally to this work.

Supporting information for this article is available on the WWW under https://doi.org/10.1002/cssc.202001355

The electrochemical properties of NICs are mainly determined by the type of electrode material and electrolyte.[6] AC is considered as a suitable cathode material owing to the excellent features like high specific surface area, tailored porosity, and excellent electrical conductivity.[7] The anode material should possess sizable channels to host the Na^+ ions, surface-controlled pseudo-capacitance-type charge storage to enhance the intercalation–deintercalation phenomena, and reduced diffusion resistance to advance the reaction kinetics. Thus far, different materials, such as carbonaceous materials (hard carbon),[8] metal oxides (V_2O_5),[9] transition metal compounds (TiO_2, Na_2TiO_3, $NiCo_2O_4$),[10] conductive MXene nanosheets,[11] and NASICON-type materials [$Na_3V_2(PO_4)_3$][12] and $NaTi_2(PO_4)_3$][13] have been extensively studied in the presence of traditional carbonate-based electrolyte as battery-type electrodes in NIC.[14] Among these, carbon-based materials can be used as both anode and cathode in Na-based ESS due to excellent chemical stability, high electrical conductivity, flexible structure, and inexpensive nature.[15] Hard carbon is one of the traditional carbonaceous material and is capable of delivering high capacity ($\approx$200 mAh g^{-1}) with moderate stability. In addition, alloying and conversion reactions generally cause structural degradation of electrode material as a result of unrelenting volume expansion. NIC has received much interest since Kuratani et al.[16] reported the possibility of fabricating the NIC with sodiated hard carbon and AC electrodes in 2012.

The typical anode, graphite in the commercialized LIBs, is reported as "not suitable" for Na intercalation as a result of the factors such as the well-defined layered structure of graphite, the large size of Na^+ ion, and thermodynamic instability of binary graphite intercalation compounds (b-GIC). Intercalation of Li^+ ions into graphite forms LiC_6 as final stoichiometry with a capacity of 372 mAh g^{-1} whereas Na-ion intercalation takes place with limited capacity (30 mAh g^{-1}).[17] According to density functional theory (DFT),[18] in comparison with Li and K, Na has a weaker binding with graphite, which is responsible for the higher formation energy of graphite–sodium-based GICs,[19] and hence, the formation of Na_xC_6 is not energetically favorable. However, Jache and Adelhelm[20] reported the possibility of Na-ion storage in graphite using co-intercalation phenomena. Afterward, Kim et al.[21] further investigated the staging mechanism of solvated Na^+ ion intercalation in graphite. Besides, ether-based electrolytes (stable at a potential below $\approx$4 V vs. Na/Na^+) are capable of prompting the co-intercalation of Na-ions with an ether solvent into graphite forming a ternary graphite intercalation compound (t-GIC).[22] It is also reported that ether-based electrolytes form a thinner solid–electrolyte interphase (SEI) layer on the anode and, hence, exhibit higher initial coulombic efficiency in comparison with ester-based electrolytes.[22a] Recently, Jache et al. also reported the formation and stability of t-GICs and made a comparison in the performance of different linear glymes.[23] Moreover, Xu et al.[17b] studied the factors affecting the co-intercalation potential of graphite and also investigated the correlation among co-intercalation voltage, solvent species, the concentration of electrolyte, and temperature to tune the sodium intercalation potential in graphite. The complexity of co-intercalation phenomena and lack of knowledge regarding how and when intercalation of Na occurs in graphite impedes the development of NICs with graphite anode. This eventually encouraged us to investigate the fabrication of such high-performance hybrid configurations using graphite as a negative electrode.[21,24]

Herein, we explore the possibility of fabricating the high-energy NIC with recovered graphite (RG) from spent LIB as anode material and commercial AC cathode for the first time with the aim of targeting low-cost, high-energy charge storage devices. The co-intercalation of solvated Na^+ ions into RG was studied with 0.5 M $NaPF_6$ in the ether-based electrolyte (TEGDME, tetraglyme, G4). Thus, formed NIC showed moderate energy and power density with superior cycling stability. In addition, the performance and durability of fabricated NICs were also tested at low and high temperatures. Also, the impact of the aging process in the cell and electrode levels were studied and compared.

Results and Discussion

The crystal structure of RG was characterized by X-ray diffraction (XRD). Figure 1a displays the XRD profile of RG, which shows a sharp diffraction peak centered at 26.26° corresponding to the crystallographic (002) plane of 2H (ABA…) phases of graphite.[25] In addition, the profile also shows a weak reflection at 54° matching the (004) plane of graphite. Raman spectra of RG presented both a weak D band at approximately 1356 cm^{-1} and a strong G band at approximately 1585 cm^{-1} (Figure 1b). The ratio of intensities between D and G band ($I_D/I_G = 0.21$) indicates a highly ordered structure of RG with less defect concentration [$I_D/(I_G+I_D) = 0.17$].[8a] The surface features of RG were verified using X-ray photoelectron spectroscopy (XPS) measurement (Figure S_1) as it is directly regenerated from spent LIBs, comprising two high-intensity peaks corresponding to C 1 s and O 1 s. The peaks appeared at 1000 and 200 eV, corresponding to Auger peaks arising from X-ray-induced Auger emission. Figure 1c illustrates that the deconvoluted C 1 s spectrum exhibits a dominating peak at 284.6 eV corresponding to sp^2-carbon, and the other peaks at 285.9 and 287.6 eV are attributed to sp^3-carbon and C=O species, respectively. The O 1 s spectrum of RG (Figure 1d) displays three peaks at 532.3 (C–O), 533.7 (O–C=O), and 530.7 eV (C=O).[26] The obtained results clearly indicate that the RG from spent LIBs shows a stable crystal structure with minimal defects and only carbon (C 1s) and oxygen (O 1s) surface functionalities similar to that of commercial graphite sample. The surface morphology and detailed microstructure of RG were explored by field-emission scanning electron microscopy (FESEM) and high-resolution transmission electron microscopy (HRTEM) analysis. Figure 2a, b shows spheroidal graphite particles of different sizes with flaky morphology. Also, the clear lattice fringes retain an inter-planar spacing of 0.34 nm, as seen from HRTEM images, indicating the layered structure of RG, as shown in Figure 2c. Further, the selected area electron diffraction (SAED) pattern (at the inset) displays two sets of bright diffraction spots in a hexagonal

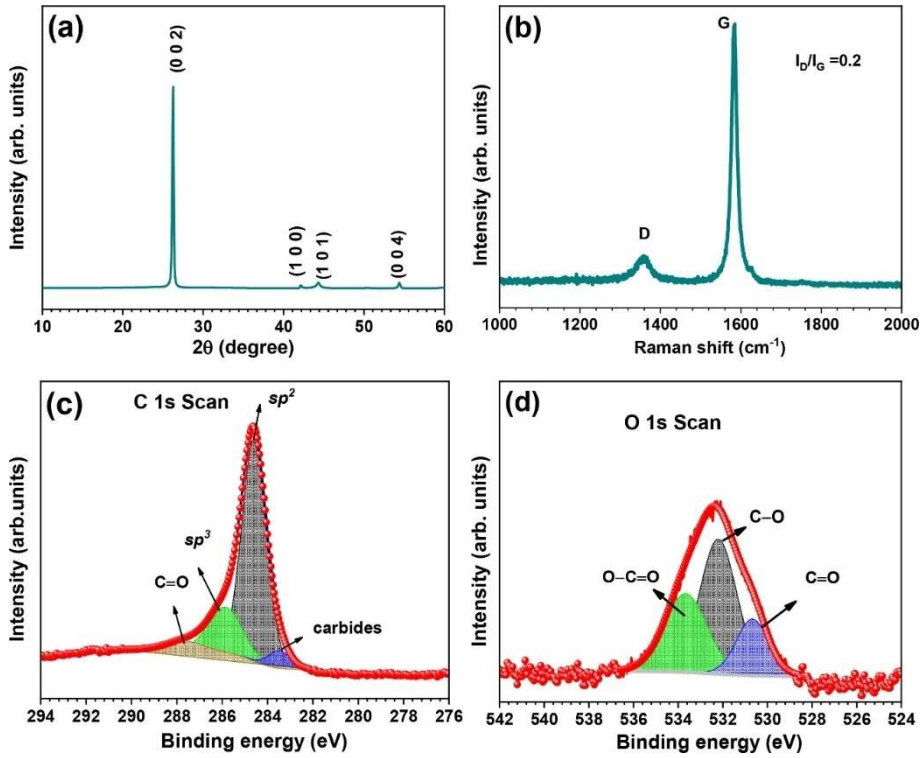

Figure 1. XRD (a), Raman (b), XPS (c, d) results of RG from spent LIBs.

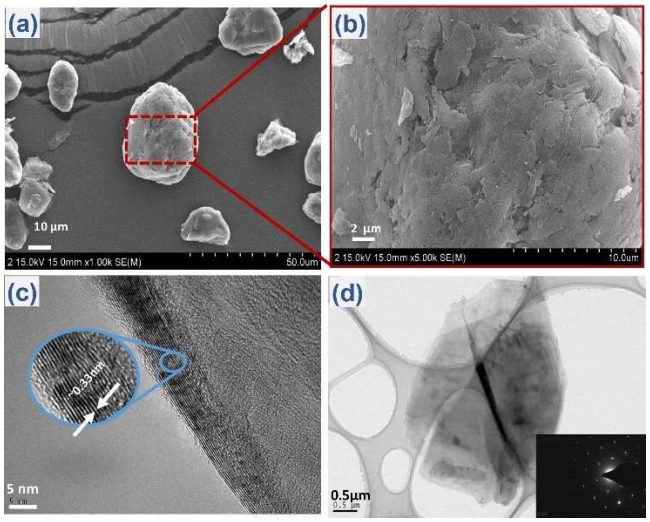

Figure 2. SEM images of RG (a, b), TEM of RG (c), and HRTEM image with SAED pattern at the inset (d).

pattern, showing the crystallinity of characteristic graphitic phase (Figure 2d).

The electrochemical performance of RG powder as an anode for NIC was investigated using a CR 2016-coin cell by employing Na metal foil as a counter electrode with 0.5 M $NaPF_6$ in TEGDME (G4) electrolyte. The desolvation activation energy of Na is anticipated to be approximately 2.5 times lower than those of Li salts, credited to feeble Lewis acidity of Na.[27] In addition, Na electrolytes are more conductive than Li. Hence, the molarity of electrolytes was limited to 0.5 M for electrochemical studies for most of the Na-based systems. Desolvation energy is directly related to Na-ion transport into the RG electrode. The mass loading of the RG electrode was limited to 3 mg for all electrochemical studies. The assembled half cells RG | 0.5 M $NaPF_6$ in TEGDME | Na showed an open circuit potential approximately 2 V vs. Na/Na^+. The cell reaction can be represented as shown in Equations (1) and (2):

$$\text{Anode}: \quad Na + [G_4] \rightleftarrows [Na - G_4]^+ + e^- \tag{1}$$

$$\text{Cathode}: \quad RG + [Na - G_4]^+ + e^- \rightleftarrows [Na - G_4]\ RG \tag{2}$$

$[Na\text{-}G_4]^+$ represents solvated Na ions and $[Na\text{-}G_4]$ RG is recovered graphite sodium intercalation compound or ternary graphite intercalation compound (t-GIC). Galvanostatic charge-discharge (GCD) cycling was performed within the potential window of 0.005–2.5 V vs. Na/Na^+ to study the co-intercalation phenomena in RG, and the performance was also compared with that of commercial graphite (CG). Figure S_2 presents the comparison of differential capacity profile and cyclic stability of RG with CG, and it confirms the performance of RG is analogous to CG. Figure 3a shows a typical cyclic voltammetry (CV) profile of RG at a scan rate of 0.1 mV s^{-1}, containing highly reversible oxidative and reductive peaks representing sodium storage in RG. The sodium storage mechanism in RG was studied with CV at different scan rates ranging from 0.1 to 5 mV s^{-1}, as demonstrated in Figure 3b. The linear variation of peak current

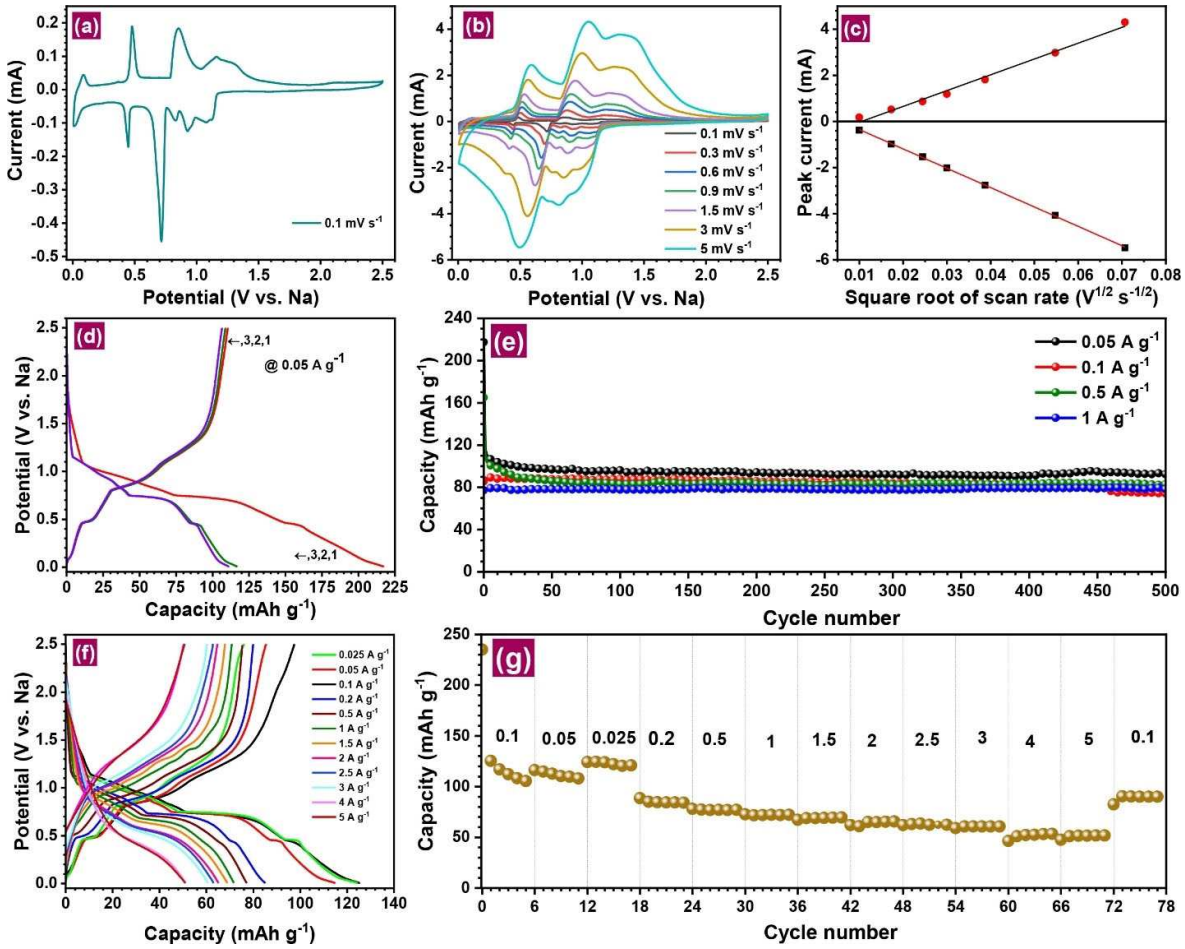

Figure 3. Electrochemical performance of RG anodes in half cell assembly with 0.5 M $NaPF_6$ in TEGDME. a) CV profile at 0.1 mV s^{-1}. b) CV profiles at various scan rates ranging from 0.1–5 mV s^{-1}. c) Plot of cathodic and anodic peak current versus square root of scan rate. d) Galvanostatic charge - discharge profiles at 0.05 A g^{-1}. e) Cyclic performance at different current rates. f) Galvanostatic charge - discharge profiles at different current rates. g) Rate performance.

with the square root of the scan rate can be seen in Figure 3c. Also, the charge-discharge profile illustrates the stepwise redox reaction revealing a stage evolution mechanism of co-intercalation phenomena in the TEGDME electrolyte. Figure 3d shows the capacity–voltage profile of RG in a 0.5 M $NaPF_6$-TEGDME electrolyte system at 50 mA g^{-1} within the potential window of 0.005–2.5 V vs. Na/Na^+, which delivered a discharge capacity of approximately 220 mAh g^{-1} with initial coulombic efficiency of approximately 50%. The lower coulombic efficiency of RG anode refers to SEI layer formation, whereas increased coulombic efficiency from the second cycle onwards indicates intercalation-deintercalation of solvated sodium ion is not limited by the formed SEI layer. In the second cycle, the cell showed the discharge capacity of approximately 115 mAh g^{-1} with $>99.9\%$ coulombic efficiency. The shape of the discharge profile was similar to previously studied graphite-based systems.[22b,23,24,28] It contains flat and sloping plateaus, which can be explained by the difference in energy between high- and low-stage GICs. During the initial stages of intercalation, the formation of high-stage GICs is represented as the sharp decreasing potential region of the voltage profile. As the intercalation process continues, the appearance of sloping and flat plateaus indicates the formation of stage-one GIC from other higher-stage GICs. The excellent electrochemical performance of RG was compared with CG; both showed similar performance in the given salt electrolyte system (Figure S_3). Figure 3e demonstrates the cyclic stability of RG at different current rates, establishing the superior cyclic stability of the cells. The rate performance of the RG half-cell was studied at various current rates (0.025–5 A g^{-1}), and the specific capacity tends to drop with an increase in current density, which may be interpreted by weakened diffusion of solvated Na^+ ions in the plateau areas. The discharge capacities were in the range of 125–52 mAh g^{-1} for various current rates, and it is also noted that the reversible capacity can be restored to the original value when current returns back to a lower rate after cycling (six cycles each) at higher current rates (Figure 3f, g). This scenario represents the integrity of the RG electrode during repeated sodiation and de-sodiation and also denotes the excellent reversibility of the insertion host along with the solvent co-intercalation. The differential capacity curve derived from the charge - discharge profile clearly presents the anodic and

cathodic peaks at corresponding voltages, as shown in Figure S_2. The rate performance of CG was also studied and presented in Figure $S_{3c,d}$. The prominent cathodic peak representing co-intercalation voltage was found to be approximately 0.75 V vs. Na/Na^+, in which the insertion potential can be adjusted by altering glyme chain length.[17b,29]

We also made an attempt to assess the electrode kinetics and Na storage property of RG using CV data at various scan rates (0.1–5 $mV s^{-1}$). When the scan rate increases, the cathodic peaks move to a low-potential region with a rise in peak intensity (Figure 3b), and it is also noticed that the intensity of peak current varies linearly with the square root of the scan rate, which indicates a diffusion-controlled process as can be seen from Figure 3c. The intercalation and de-intercalation of $[Na\text{-}G_4]^+$ is a diffusion-controlled process, and the apparent diffusion coefficient was calculated by the Randles–Sevcik equation and was found to be 1.733×10^{-7} and 1.156×10^{-7} $cm^2 s^{-1}$ based on cathodic and anodic peak current, respectively (Figure 3c). However, the values are higher than the reported value of $1–6\times10^{-10}$ $cm^2 s^{-1}$, which may be due to lower concentration of electrolyte.[30] The contributions of diffusion-limited intercalation and pseudocapacitive intercalation in sodium storage were qualitatively calculated by using the power-law equation ($i=av^b$), which gives the relationship between measured current i [A] and scan rate v [$mV s^{-1}$] from CV profiles. Here, a and b are adjustable parameters, and the value of b can be found from the slope of log i vs. log v plot. At a value of $b=0.5$, the current response is expected to be a diffusion-controlled faradaic process, and $b=1$ indicates the supremacy of the capacitive process. The cathodic peaks were labeled as C_1, C_2, C_3, C_4, and C_5 for the CV profile at 0.1 $mV s^{-1}$, as illustrated in Figure S_{4a}. The b values for the peaks are estimated as 0.89, 0.9, 0.93, 0.6, and 0.7, respectively (Figure S_{4b}). For all the peaks, the b value is higher than 0.5, which indicates the combination of capacitive (intercalation pseudocapacitance) and diffusion-controlled intercalation mechanism. The behavior of pseudocapacitance in the RG electrode is owing to the intercalation of solvated ions, $[Na\text{-}G_4]^+$ ions, into the open channels, or the van der Waals gap of RG that makes it considered as a non-faradaic reaction. The b value of C_4 is estimated to be 0.6, which provides an indication that the diffusion-controlled intercalation mainly takes place at this peak, corresponding to a potential of approximately 0.75 V vs. Na/Na^+. The peaks C_1, C_2, and C_3 hold the value of b in the range of 0.8–0.93, indicating the increased contribution of pseudocapacitance. Based on these values, the percentage contribution of capacitive and diffusion-controlled elements has been calculated for different peaks, and the discharge profile was divided into three regions as I (C_1, C_2, C_3), II (C_4), and III (C_5). For region II, approximately 79% diffusion-limited intercalation and 15% pseudocapacitive intercalation were estimated, whereas for the regions I and III, 95 and 29% capacitance and 5 and 71% diffusion-controlled intercalation were calculated, respectively. This estimation is based on the following Equation (3):

$$i = k_1 v + k_2 v^{1/2} \quad (3)$$

Here, k_1 and k_2 are constants, v is the scan rate, and $k_1 v$ and $k_2 v^{1/2}$ represent the capacitive and intercalation elements.

In addition, the contribution ratio of two different Na storage mechanisms was determined for different scan rates varying from 0.1–1.5 $mV s^{-1}$, as presented in Figure S_5. It is observed that the increase in scan rate results in an increase of intercalation pseudocapacitance contribution in the total storage mechanism. To further confirm the suitability of the RG electrode for Na storage, electrochemical impedance spectroscopy (EIS) was performed. The Nyquist plots of fresh cell and the cell after cycling are presented in Figure S_6. The fresh cell shows smaller charge-transfer resistance (R_{ct}), solution resistance (R_s), and a low-frequency tail represents the Warburg diffusion element caused by the diffusion-controlled process. The EIS spectrum for the cell after cycling illustrates further decreased R_{ct} and R_s, indicating that the electrode is activated; it becomes more accessible to the electrolyte, and there is no degradation of the electrode material. The cell exhibits small Warburg impedance, representing the fact that at higher frequencies, the diffusing reactant does not have to move very far. These factors could help to achieve excellent cyclability of the RG electrode with thin SEI layer formation as solvated ions are able to pass through it with negligible charge-transfer resistance. The half-cell (RG vs. Na) performance shows excellent stability and low internal resistance of Na-based systems.

Mere half-cell performance is not sufficient to claim the potential application of the material irrespective of the electrode (negative or positive) and configuration (battery or capacitor). In this line, we wanted to study the possibility of employing such RG as a battery-type electrode towards building the high-energy and high-power charge storage device, NIC with AC as a counter electrode. To date, to the best of our knowledge, the utilization of such glyme family electrolytes is not employed in full-cell or practical assemblies. As mentioned in the introduction, the hybrid assembly is anticipated to translate both high-energy and high-power capability in a single assembly. Prior to the fabrication of the NIC, the mass balance between the electrodes is very crucial to maximize the utilization of the active materials. Accordingly, the supercapacitor-type AC was employed as a cathode for NIC configuration. The performance of the AC electrode was also tested in a CR 2016-coin cell assembly with Na metal foil as a counter electrode using 0.5 M $NaPF_6$ in the TEGDME electrolyte to estimate the charge balance between anode and cathode. The assembled half cells AC | 0.5 M $NaPF_6$ in TEGDME (G4) | Na showed an open circuit potential of approximately 2.95 V vs. Na/Na^+. The GCD cycling at 50 $mA g^{-1}$ within the voltage window of 1.5–4.2 V vs. Na/Na^+ exhibits an initial discharge capacity of approximately 74 $mAh g^{-1}$ (specific capacitance = 93.5 $F g^{-1}$) with nearly 100% capacity retention after 75 cycles (Figure S_7). The cyclic stability was also tested at 100 $mA g^{-1}$, which delivered approximately 95% capacity retention after 200 cycles (Figure S_8). The rectangular CV traces of the half-cell shown in Figure S_{10a} denote the ideal capacitive behavior of the AC electrode.

A dual-carbon NIC was fabricated by using pre-sodiated RG electrode as the anode, commercial AC electrode as the

cathode, Whatman paper as a separator, and 0.5 M $NaPF_6$ in TEGDME as the electrolyte. The pre-sodiation of the RG electrode was carried out with the help of Swagelok fittings with Na metal foil as a counter electrode. During the charge - discharge cycle, the intercalation and de-intercalation of solvated Na ion ($[Na\text{-}G_4]^+$) takes place in the RG electrode. Under the discharged conditions [i.e., with intercalated ($[Na\text{-}G_4]^+$) ions], the cell was dismantled, and the sodiated RG electrode was paired with the AC electrode of optimum mass loading. Keeping the specific capacities of both electrodes in mind, AC at 1.5–4.2 V vs. Na/Na^+ (74 mAh g^{-1} at 50 mA g^{-1}) and RG at 0.005–2.5 V vs. Na/Na^+ (115 mAh g^{-1} at 50 mA g^{-1}), the NIC was assembled with anode and cathode in the mass ratio of approximately 1:1.6. The mass loading of the anode and cathode electrode was adjusted to approximately 1.7 and 2.7 mg cm^{-1}, respectively. The near-rectangular-shaped CV with small redox peaks specifies the performance of NIC with the combination of two different charge-storage mechanisms within the potential window 1–3.75 V. Figure 4a represents the CV profile of assembled NIC at 0.1 mV s^{-1}. The GCD analysis was performed at different current densities from 0.025 to 3 A g^{-1}, and the charge - discharge curves exhibiting near-linear behavior indicate the typical hybrid capacitor performance, as evident from Figure 4b,c. The gravimetric energy and power density of the assembled NIC were calculated based on the total mass of active material in both the electrodes (≈6.5 mg) using the standard equations (see the Supporting Information). The high energy density of 59.93 Wh kg^{-1} was achieved at a power density of 57.2 W kg^{-1} when the cell was subjected to a low current density of 0.025 A g^{-1} at ambient conditions. As well, we could observe the stable energy densities above 55 Wh kg^{-1} at low current densities with an increase in power density with respect to the applied current. Additionally, the cell could deliver a maximum power density of 6.84 kW kg^{-1} with an energy density of 12.58 Wh kg^{-1}. The dual-carbon NIC fabricated in the presence of glyme family solvents with a pre-sodiated RG electrode as the anode and AC electrode as the cathode functions by the combination of different charge-storage mechanisms. During the charge - discharge process, both pseudocapacitive intercalation/de-intercalation and diffusion-limited intercalation/de-intercalation reaction take place at the RG electrode for reversible storage of sodiated Na-ions. Parallelly, the adsorption and desorption of PF_6^- and Na-ions from electrolyte takes place at the AC cathode. The Nyquist plot obtained from EIS measurements for the NIC device is given in Figure S_9, and the inset displays the corresponding equivalent circuit model created by the Z-fit technique. The radius of the semicircle reflects reaction kinetics, which is based on R_{ct}. The

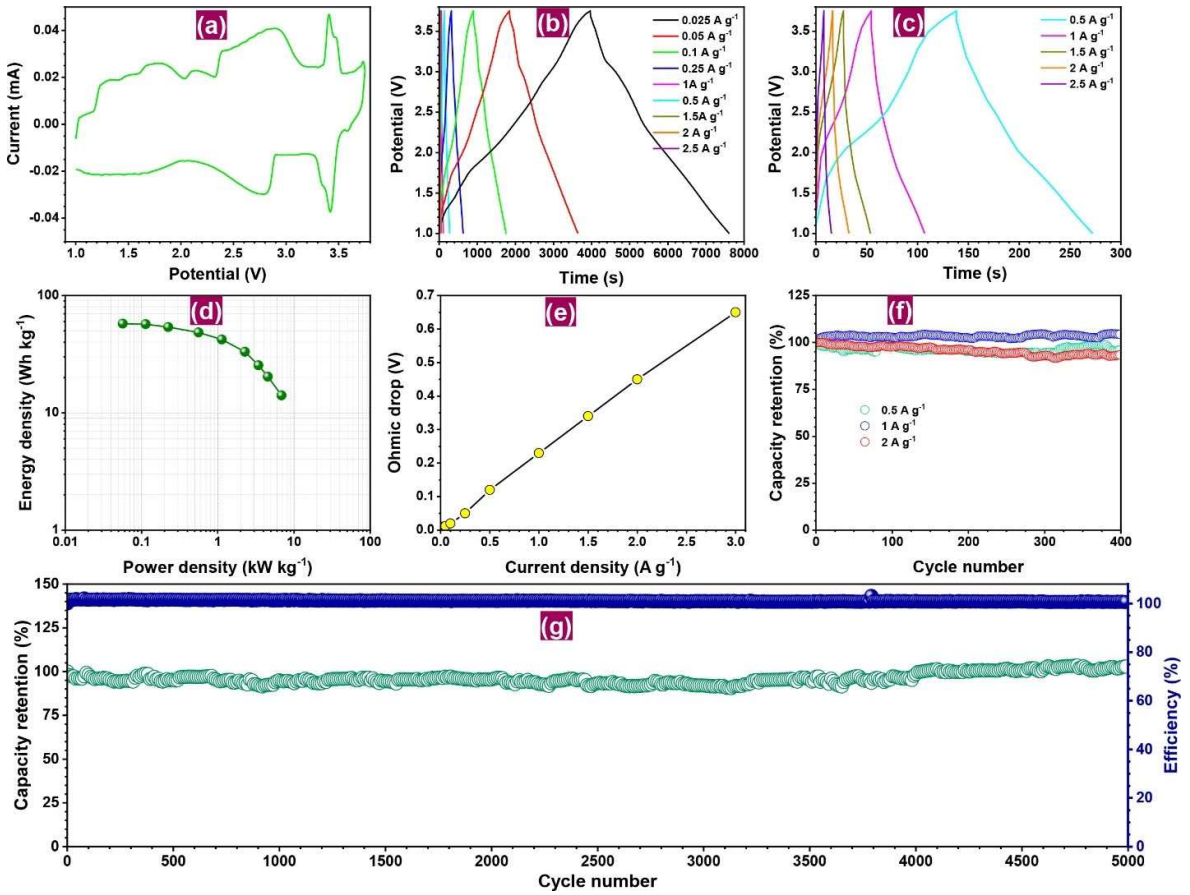

Figure 4. Electrochemical performance of AC/RG NIC assembly with 0.5 M $NaPF_6$ in TEGDME. a) CV profile at 0.1 mV s^{-1}. b,c) Galvanostatic charge - discharge profiles at various current densities (0.025–3 A g^{-1}). d) Ragone plot of fabricated NIC. e) *IR* drop versus applied current density. f) Cyclic stability of fabricated NIC at different current rates. g) Long-term cyclability of assembled NIC at 0.5 A g^{-1} between the potential window of 1–3.75 V.

slope of a line in the low-frequency region corresponds to diffusion resistance of solvated Na-ions in the electrolyte. The low values of equivalent series resistance (ESR) and R_{ct} implies a fast charge - discharge capability of NIC.

Figure S_{10} depicts the CV profiles of NIC, along with the half-cells of both RG and AC. Figure 4d represents the Ragone plot of assembled NIC that exposed a higher energy density of 59.93 Wh kg^{-1} at 57.2 W kg^{-1}. Moreover, we compared the electrochemical performance with some other previously reported Li/Na-based hybrid charge storage devices (Figure S_{11}), and it can be seen clearly that our NIC device outperformed other configurations, for example, AC/Na_2CoSiO_4 (NIC, 12.4 Wh kg^{-1} @ 782.7 W kg^{-1}),[31] $NiCo_2O_4$/AC (NIC, 13.8 Wh kg^{-1} @ 308 W kg^{-1}),[32] Nb_2O_5/AC (LIC, 40 Wh kg^{-1} @ 300 W kg^{-1}),[33] V_2O_5-carbon nanotubes (CNT)/AC (LIC, 40 Wh kg^{-1} @ 210 W kg^{-1}),[34] V_2O_5-CNT/AC (NIC, 38 Wh kg^{-1} @ 140 W kg^{-1}),[35] γ-$Li_xV_2O_5$/AC (LIC, 43.98 Wh kg^{-1} @ 280 W kg^{-1}),[36] Nb_2O_5/peanut shell carbon (PSC) (NIC, 43.2 Wh kg^{-1} @ 160 W kg^{-1}),[37] MoS_2-C/graphite (NIC, 46.3 Wh kg^{-1} @ 910 W kg^{-1}),[38] and sodium titanate nanotubes (Na-TNT)/AC (NIC, 34 Wh kg^{-1} @ 889 W kg^{-1}).[39] Figure 4e represents the plot of ohmic drop versus applied current density, which specifies the linear increase in ohmic drop with a rise in applied current density. The cyclic stability of the hybrid device using RG as an anode at different current densities of 0.5, 1, and 2 A g^{-1} could retain approximately 95.8, 104.3, and 93.27% of the initial capacity after 400 cycles (Figure 4f). Furthermore, the long-term cyclability of NIC was tested at 0.5 A g^{-1}, showing that the fabricated NIC using RG as the anode material can maintain more than 98% of the initial capacity value with >99.9% coulombic efficiency even after 5000 cycles as presented in Figure 4g. The charge/discharge duration of fabricated NIC at 1 A g^{-1} is observed as approximately55 seconds.

In addition, the effect of temperature on the performance of RG/AC-based NIC was tested at four different temperature conditions (−5, 10, 25, and 50 °C). Figure 5a represents the GCD

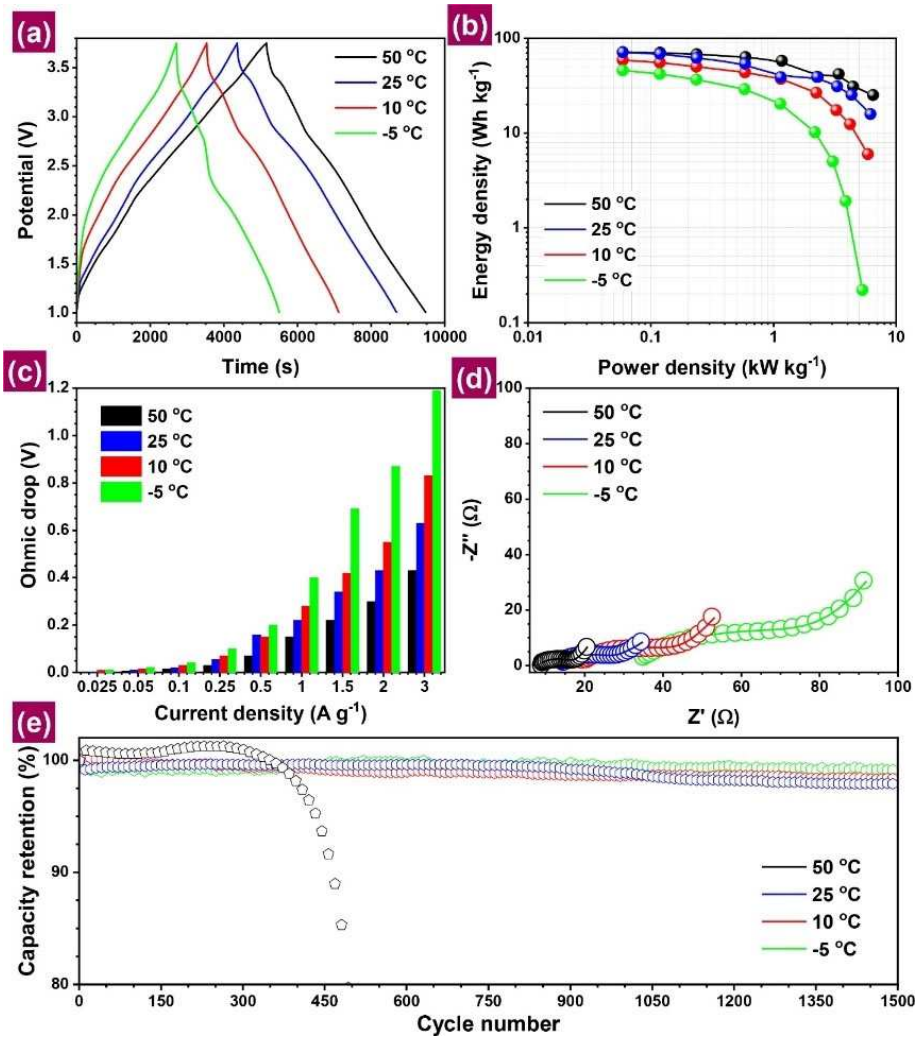

Figure 5. Effect of temperature on the performance of AC/RG NIC coin cell assembly with 0.5 M $NaPF_6$ in TEGDME. a) Galvanostatic charge - discharge profiles at 0.025 A g^{-1} for different temperature conditions (−5, 10, 25, 50 °C). b) Ragone plot of AC/RG NIC at various temperature conditions. c) Plot of *IR* drop versus current density at different temperature. d) EIS traces of fabricated NIC before cycling at different temperature conditions. e) Cyclic stability in different temperature at current density of 0.5 A g^{-1}.

profiles at 0.025 A g^{-1} for all four temperature conditions. At high temperature, the charge - discharge time is higher than that at ambient conditions; however, the cell exhibits a fast charge - discharge process at low temperature. Additionally, the voltage versus charge - discharge time profile for the NIC at different temperature conditions is illustrated in Figure S_{12}. Figure 5b symbolizes the Ragone plot, which acquires the performance comparison of single NIC at different temperatures in terms of energy and power density. Initially, the performance of fresh NIC was tested at 50 °C, which could deliver a maximum energy density of 71.3 Wh kg^{-1} @ 0.059 kW kg^{-1}. The same cell was tested at different temperatures after giving a rest time of 4 h to attain a stable temperature within the chamber. Interestingly at 25 °C, the cell could deliver an energy density of 71.27 Wh kg^{-1}. The performance was superior to the performance of the fresh cell at ambient conditions, with an increase in the value of energy density by approximately 19% (Figure S_{13}). This can be due to the initial thermal activation of NIC at high temperature, which surpasses the traditional electrode heat-treating approaches.[40] Further, the performance was tested at 10 and −5 °C, and the cell delivered a maximum energy density of 58.95 and 45.89 Wh kg^{-1}, respectively. It can be seen that the cell at low power densities could deliver nearly stable performance irrespective of the temperature conditions, but when the power density increased, the cell performance started diminishing. This is because of the increased viscosity of electrolyte, which hinders the facile mobility of charge carriers upon the charge - discharge process.[40b,41] Figure 5c shows the variation of the ohmic drop with an increase in current density. Apparently, at higher current density, the ohmic drop is found to be very high; also, an upward trend with a decrease in temperature is noted. The Nyquist plot of the NIC before cycling at different temperatures is given in Figure 5d, and an apparent change of impedance with temperature was observed. The radius of semicircle increases with a decrease in temperature specifies an increase in charge-transfer resistance at low temperatures, and a decrease in temperature increases the resistance of the electrolyte solution (R_s). The cycling stability of the same NIC was tested at different temperatures starting from −5, 10, 25, and 50 °C at 0.5 A g^{-1}, and the device could deliver approximately 98% capacity retention even after 1500 cycles at all temperature conditions except 50 °C. At this high temperature, a drastic fade in the capacity is observed after 300 cycles. The cyclic stability of NIC at high temperature was further confirmed by testing a fresh cell at 50 °C, and its capacity variation with respect to cycle number was observed. After 600 cycles, a sudden decrease in capacity value was observed at 0.5 A g^{-1}, whereas a gradual decrease in capacity throughout cycle life was seen at 1 A g^{-1} (Figure S_{14}). This confirms the poor stability of NIC cells at high temperatures, and that can be explained by the fact that the electrochemical stability window of the electrolyte decreases with increasing temperature.[40b]

Conclusions

For the first time, we have demonstrated the assembly of a cost-effective, dual-carbon electrode Na-ion capacitor (NIC) with high energy, power, and a long lifetime by employing recovered graphite (RG) from spent lithium ion batteries (LIBs) as anode and commercial activated carbon (AC) as the cathode using ether-based electrolyte. The efficient recovery process of graphite has been carried out with simple ultrasonic leaching using the green solvent water, and the crystallinity of the RG was also confirmed even after more charge - discharge cycles that pave a way to reuse it as anode for NIC. The electrode kinetics and sodium storage property of the RG electrode was studied in half-cell assembly in conjunction with the concept of co-intercalation phenomena. Moreover, the percentage contribution of intercalation pseudocapacitance and diffusion-controlled intercalation involved in the Na storage mechanism of the RG electrode was discussed in detail in this study. The fabricated RG (pre-sodiated)/AC could deliver a maximum energy density of 59.93 Wh kg^{-1} and a maximum power of 6.8 kW kg^{-1} with approximately 98% capacity retention even after 5000 cycles at ambient temperature conditions. Furthermore, the influence of temperature on the electrochemical performance of the hybrid device was also inspected and confirms an excellent performance of the balanced NIC assembly. Therefore, this novel concept of building cost-effective high-performance NIC by engaging RG as the anode in the next-generation energy storage devices undoubtedly contributes to attaining a sustainable environment with less energy crisis and reduced waste.

Experimental Section

Recovery of graphite from spent LIBs

The spent LIBs of mobile phones from different sources (local service centres) were collected irrespective of manufactures and submerged in NaCl solution for a whole day with the aim of completing the discharge process to avert any risk during battery dismantling.[42] The anode part (Cu-foil with graphite paste) was separated from the cathode (Al foil containing Li-based metal oxide), separator, metallic cases, and other parts to reuse the graphite directly as an anode in the fabrication of the hybrid capacitor. At the beginning of the sonication process, deionized water was used to separate the graphite paste from the Cu foils as well as to collect the presence of "Li" on the surface of recovered graphite from the SEI layer, which is formed due to the continuous charge - discharge cycles. Further, stickier graphite paste on the Cu foil was recovered fully with a little amount of dimethylformamide (DMF) solvent, washed with water, and dried in an oven. The Brunauer–Emmett–Teller (BET) specific surface area of the recovered graphite was found to be approximately 11.7 $m^2 g^{-11}$ (Figure S_{15}).

Material characterization

SEM (S-4700, Hitachi, Japan) and HRTEM (JEM-2000, EX-II, JEOL, Japan) were used to observe the surface morphology and microstructure of RG. XRD (ULTIMA-IV, Rigaku, ARBL-RAD) was performed

with monochromatic CuK_α radiation ($\lambda = 0.15406$ nm) at a scanning rate of $1^\circ min^{-1}$ to analyze the crystallinity and phase of the material. Purity and structural properties were further investigated with Raman spectroscopy (LabRam HR800 UV Raman microscope, Horiba Jobin- Yvon, France) using 515 nm diode laser as an excitation light source. The surface oxidation states of the sample were identified by XPS (Multilab 2000, UK).

Fabrication of cells

The RG (80%) was mixed with 10% conductive carbon (acetylene black), 10% polyvinylidene fluoride (PVDF) binder, and *N*-methyl pyrrolidone (NMP) solvent to obtain a homogeneous slurry. The slurry was kept under constant stirring overnight to get uniform mixing, and further, it was coated on to Cu-foil using a doctor blade. The slurry coated Cu-foils were dried overnight and then pressed under a hot roll press (Tester Sangyo, Japan). Disc electrodes with a diameter of 14 mm were punched out, and the mass of active material in each disc was within the range of 2 mg. The cathode half-cell electrode was made by mixing the AC (YP-80F, Kuraray, Japan), conductive carbon (acetylene black), and binder [teflonized acetylene black (TAB-2)] in the ratio of 80:10:10 using the solvent ethanol with the help of mortar and pestle. The thin layer of electrode material was pressed on a 16 mm diameter stainless-steel mesh current collector (Goodfellow, UK), and further electrodes were dried at 75 °C in a vacuum oven for 4 h. Both the half cells and NICs were fabricated into coin cell assembly (CR 2016) in Ar filled glove box using 0.5 M $NaPF_6$ (98%, Sigma Aldrich) in TEGDME electrolyte and Whatman paper (1825-047, GF/F) separator. The preparation of electrolytes was also done in the glovebox to prevent water contamination. The half-cells were assembled with AC/RG electrodes and Na metal foil as the counter electrode. Swagelok cells were used for the pre-sodiation of graphite electrodes, which was used as the anode in NIC along with AC cathodes.

Electrochemical measurements

The electrochemical performance of half cells and NICs were tested with a battery tester, BCS 805 (Biologic, France). EIS was executed for half-cells (AC/Na), (RG/Na), and NICs at an AC voltage of 10 mV in the range of 10 kHz to 1 Hz. Galvanostatic charge - discharge studies were done within the voltage window of 0.005–2.5 V for RG/Na half-cell, 1.5–4.2 V for AC/Na half-cell, and 1–3.75 V for NICs. CV tests were performed at different scan rates for both half cells and NICs. The environmental chamber (Espec, Japan) was used for testing the low- and high-temperature performance of assembled NICs.

Acknowledgments

MLD wishes to thank the funding through Women Scientist Scheme-B (DST/WOS-B/2018/2039) from the KIRAN division of the Department of Science & Technology (DST), Govt. of India. YSL acknowledges the financial support from the National Research Foundation of Korea (NRF) grant funded by the Korea government (Ministry of Science, ICT & Future Planning) (No. 2019R1A4A2001527). VA acknowledges financial support from the Science & Engineering Research Board (SERB), a statutory body of the Department of Science & Technology, Govt. of India, through the Ramanujan Fellowship (SB/S2/RJN-088/2016).

Conflict of Interest

The authors declare no conflict of interest.

Keywords: Graphite · ether · high-temperature aging · Na-ion capacitor · pre-sodiation

[1] a) Z. P. Cano, D. Banham, S. Ye, A. Hintennach, J. Lu, M. Fowler, Z. Chen, *Nat. Energy* **2018**, *3*, 279–289; b) M. Guarnieri, in *2012 Third IEEE HISTory of ELectro-technology CONference (HISTELCON)*, **2012**, pp. 1–6.
[2] a) H. Wang, C. Zhu, D. Chao, Q. Yan, H. J. Fan, *Adv. Mater.* **2017**, *29*, 1702093; b) V. Aravindan, J. Gnanaraj, Y.-S. Lee, S. Madhavi, *Chem. Rev.* **2014**, *114*, 11619–11635.
[3] S. Natarajan, V. Aravindan, *Adv. Energy Mater.* **2018**, *8*, 1802303.
[4] a) P. Adelhelm, P. Hartmann, C. L. Bender, M. Busche, C. Eufinger, J. Janek, *Beilstein J. Nanotechnol.* **2015**, *6*, 1016–1055; b) V. Aravindan, M. Ulaganathan, S. Madhavi, *J. Mater. Chem. A* **2016**, *4*, 7538–7548; c) K. Subramanyan, V. Aravindan, *Chem* **2019**, *5*, 3096–3126.
[5] a) J.-Y. Hwang, S.-T. Myung, Y.-K. Sun, *Chem. Soc. Rev.* **2017**, *46*, 3529–3614; b) Y. Liu, X. Qin, F. Liu, B. Huang, S. Zhang, F. Kang, B. Li, *ACS Nano* **2020**, *14*, 1837–1845.
[6] H. Zhang, M. Hu, Q. Lv, Z.-H. Huang, F. Kang, R. Lv, *Small* **2019**, *n/a*, 1902843.
[7] Z. Li, K. Xu, Y. Pan, *Nanotechnology* **2019**, *8*, 35–49.
[8] a) H. Liu, X. Liu, H. Wang, Y. Zheng, H. Zhang, J. Shi, W. Liu, M. Huang, J. Kan, X. Zhao, D. Li, *ACS Sustainable Chem. Eng.* **2019**, *7*, 12188–12199; b) P. Han, X. Han, J. Yao, L. Zhang, X. Cao, C. Huang, G. Cui, *J. Power Sources* **2015**, *297*, 457–463.
[9] K. Ramakrishnan, N. Chandrasekaran, R. Karvembu, V. Boddu, *Electrochim. Acta* **2017**, *256*.
[10] a) B. Babu, M. M. Shaijumon, *J. Power Sources* **2017**, *353*, 85–94; b) Z. Le, F. Liu, P. Nie, X. Li, X. Liu, Z. Bian, G. Chen, H. B. Wu, Y. Lu, *ACS Nano* **2017**, *11*, 2952–2960.
[11] a) X. Wang, S. Kajiyama, H. Iinuma, E. Hosono, S. Oro, I. Moriguchi, M. Okubo, A. Yamada, *Nat. Commun.* **2015**, *6*, 1–6; b) S. Kajiyama, L. Szabova, K. Sodeyama, H. Iinuma, R. Morita, K. Gotoh, Y. Tateyama, M. Okubo, A. Yamada, *ACS Nano* **2016**, *10*, 3334–3341.
[12] S. Wang, J. Zhao, L. Wang, X. Liu, Y. Wu, J. Xu, *Ionics* **2015**, *21*, 2633–2638.
[13] H.-K. Roh, M. S. Kim, K. Y. Chung, U. Mani, V. Aravindan, M. Srinivasan, K. C. Roh, K. B. Kim, *J. Mater. Chem. A* **2017**, *5*, 17506–17516.
[14] X. Zhao, Y. Zhang, Y. Wang, H. Wei, *Battelle Inst. Mater. Sci. Colloq.* **2019**, *2*, 899–917.
[15] a) Z. Li, K. Xu, Y. Pan, *Nanotechnology* **2019**, *8*, 35; b) S. Natarajan, Y. S. Lee, V. Aravindan, *Chem. Asian J.* **2019**, *14*, 936–951.
[16] K. Kuratani, M. Yao, H. Senoh, N. Takeichi, T. Sakai, T. Kiyobayashi, *Electrochim. Acta* **2012**, 320–325.
[17] a) W. Luo, F. Shen, C. Bommier, H. Zhu, X. Ji, L. Hu, *Acc. Chem. Res.* **2016**, *49*, 231–240; b) Z.-L. Xu, G. Yoon, K.-Y. Park, H. Park, O. Tamwattana, S. Joo Kim, W. M. Seong, K. Kang, *Nat. Commun.* **2019**, *10*, 2598.
[18] a) Z. Wang, S. M. Selbach, T. Grande, *RSC Adv.* **2014**, *4*, 4069–4079; b) B.-Q. Dai, G.-L. Zhang, *Mater. Chem. Phys.* **2003**, *78*, 304–307; c) Y. Okamoto, *J. Phys. Chem. C* **2014**, *118*, 16–19; d) K. Nobuhara, H. Nakayama, M. Nose, S. Nakanishi, H. Iba, *J. Power Sources* **2013**, *243*, 585–587.
[19] Y. Liu, B. V. Merinov, W. A. Goddard, *Proc. Natl. Acad. Sci. USA* **2016**, *113*, 3735.
[20] B. Jache, P. Adelhelm, *Angew. Chem. Int. Ed.* **2014**, *53*, 10169–10173; *Angew. Chem.* **2014**, *126*, 10333–10337 **2014**, 126, 10333–10337.
[21] H. Kim, J. Hong, G. Yoon, H. Kim, K.-Y. Park, M.-S. Park, W.-S. Yoon, K. Kang, *Energy Environ. Sci.* **2015**, *8*, 2963–2969.
[22] a) Z. Lin, Q. Xia, W. Wang, W. Li, S. Chou, *Info Chim. Mag.* **2019**, *1*, 376–389; b) Z. Zhu, F. Cheng, Z. Hu, Z. Niu, J. Chen, *J. Power Sources* **2015**, *293*, 626–634.
[23] B. Jache, J. O. Binder, T. Abe, P. Adelhelm, *Phys. Chem. Chem. Phys.* **2016**, *18*, 14299–14316.
[24] a) G. Yoon, H. Kim, I. Park, K. Kang, *Adv. Energy Mater.* **2017**, *7*, 1601519; b) J. Zhang, D.-W. Wang, W. Lv, L. Qin, S. Niu, S. Zhang, T. Cao, F. Kang, Q.-H. Yang, *Adv. Energy Mater.* **2018**, *8*, 1801361; c) Y. Li, Y. Lu, P. Adelhelm, M.-M. Titirici, Y.-S. Hu, *Chem. Soc. Rev.* **2019**, *48*, 4655–4687.

[25] M. Seehra, U. Geddam, D. Schwegler-Berry, A. Stefaniak, *Carbon* **2015**, *95*.
[26] Y. Li, Y. Yang, P. Zhou, T. Gao, Z. Xu, S. Lin, H. Chen, J. Zhou, S. Guo, *Mat. Cas.* **2019**, *1*, 893–910.
[27] K. L. Browning, R. L. Sacci, G. M. Veith, *J. Electrochem. Soc.* **2017**, *164*, A580-A586.
[28] a) R. Jia, G. Shen, D. Chen, *Sci. China Mater.* **2020**, *63*, 185–206; b) H. Kim, J. Hong, Y.-U. Park, J. Kim, I. Hwang, K. Kang, *Adv. Funct. Mater.* **2015**, *25*, 534–541.
[29] a) B. Jache, J. Binder, T. Abe, P. Adelhelm, *Phys. Chem. Chem. Phys.* **2016**, *18*; b) Z.-L. Xu, G. Yoon, K.-Y. Park, H. Park, O. Tamwattana, S. J. Kim, W. M. Seong, K. Kang, *Nat. Commun.* **2019**, *10*, 1–10.
[30] H.-J. Liang, B.-H. Hou, W.-H. Li, Q.-L. Ning, X. Yang, Z.-Y. Gu, X.-J. Nie, G. Wang, X.-L. Wu, *Energy Environ. Sci.* **2019**, *12*, 3575–3584.
[31] S. Gao, J. Zhao, Y. Zhao, Y. Wu, X. Zhang, L. Wang, X. Liu, Y. Rui, J. Xu, *Mater. Lett.* **2015**, *158*, 300–303.
[32] R. Ding, L. Qi, H. Wang, *Electrochim. Acta* **2013**, *114*, 726–735.
[33] J. Come, V. Augustyn, J. W. Kim, P. Rozier, P.-L. Taberna, P. Gogotsi, J. W. Long, B. Dunn, P. Simon, *J. Electrochem. Soc.* **2014**, *161*, A718-A725.
[34] Z. Chen, V. Augustyn, J. Wen, Y. Zhang, M. Shen, B. Dunn, Y. Lu, *Adv. Mater.* **2011**, *23*, 791–795.
[35] Z. Chen, V. Augustyn, X. Jia, Q. Xiao, B. Dunn, Y. Lu, *ACS Nano* **2012**, *6*, 4319–4327.
[36] M. L. Divya, V. Aravindan, *Chem. Asian J.* **2019**, *14*, 4665–4672.
[37] H. Li, Y. Zhu, S. Dong, L. Shen, Z. Chen, X. Zhang, G. Yu, *Chem. Mater.* **2016**, *28*, 5753–5760.
[38] L. Zhao, L. Qi, H. Wang, *RSC Adv.* **2015**, *5*, 15431–15437.
[39] J. Yin, L. Qi, H. Wang, *ACS Appl. Mater. Interfaces* **2012**, *4*, 2762–2768.
[40] a) D.-Z. Chen, J. Yu, W. Lu, Y. Zhao, Y. Yan, T.-W. Chou, *Electrochim. Acta* **2017**, *233*, 181–189; b) G. Xiong, A. Kundu, T. Fisher, *Inflammation* **2015**, 71–114; c) C. Masarapu, H. F. Zeng, K. H. Hung, B. Wei, *ACS Nano* **2009**, *3*, 2199–2206.
[41] a) E. Iwama, P. Taberna, P. Azais, L. Brégeon, P. Simon, *J. Power Sources* **2012**, *219*, 235–239; b) Y. Zhou, M. Ghaffari, M. Lin, H. Xu, H. Xie, C. M. Koo, Q. M. Zhang, *RSC Adv.* **2015**, *5*, 71699–71703; c) E. J. Brandon, W. C. West, M. C. Smart, *NASA Tech Briefs* **2008**, *32*, 32.
[42] a) S. Natarajan, V. Aravindan, *Adv. Energy Mater.* **2020**, 2002238; b) K. Subramanyan, S. Natarajan, Y.-S. Lee, V. Aravindan, *Chem. Eng. J.* **2020**, *397*, 125472; c) M. L. Divya, S. Natarajan, Y.-S. Lee, V. Aravindan, *J. Mater. Chem. A* **2020**, *8*, 4950–4959; d) M. L. Divya, S. Natarajan, Y.-S. Lee, V. Aravindan, *Small* **2020**, *10.1002/smll.202002624*.

Manuscript received: June 2, 2020
Revised manuscript received: September 1, 2020
Accepted manuscript online: September 2, 2020
Version of record online: September 17, 2020